

Dielectric Nanoparticles as Efficient RGB Sources by Second, Third, and Fourth Harmonic Generation Excited at Telecom Wavelengths

Jeremy Riporto,^{1,2} Alexis Demierre,² Gabriel Campargue,² Cédric Schmidt,² Vasyil Kilin,² Ronan Le Dantec,¹ Jean-Pierre Wolf,² Yannick Mugnier,¹ and Luigi Bonacina²

¹*Université Savoie Mont Blanc, SYMME, F-74000 Annecy, France*

²*GAP-Biophotonics, Université de Genève, 22 chemin de Pinchat, 1211 Genève 4, Switzerland*

We demonstrate the simultaneous generation of second (red), third (green), and fourth (blue) harmonic from a single dielectric Bismuth Ferrite nanoparticle excited by a telecom fiber laser at 1560 nm. We first characterize the signals associated with different nonlinear orders in terms of spectrum, excitation intensity dependence, and relative signal strengths. Successively, on the basis of the polarization-resolved emission curves of the three harmonics, we discuss the interplay of susceptibility tensor components at the different orders and we show how polarization can be used as an optical handle to control the frequency conversion properties on demand.

Keywords: harmonic generation; harmonic nanoparticles; perovskites; bismuth ferrite; frequency conversion.

The generation and control of nonlinear parametric signals at the nanoscale is paving the ways to novel applications in imaging, sensing, optoelectronics. To date, most of the research efforts have been concentrated on noble metal nanoparticles and nanostructures¹ with a focus on their second ($\chi^{(2)}$)^{2,3} and third order ($\chi^{(3)}$)^{4,5} response. Some notable exceptions include the nonlinear harmonic generation by semiconductor nanoparticles^{6,7}, two dimensional materials⁸⁻¹⁰, and noncentrosymmetric metal oxide nanoparticles (Harmonic NanoParticles, HNPs). HNPs are attracting growing interest because of their extremely high nonlinear coefficients,¹¹ and robustness of their nonlinear response which - contrary to noble metal particles - is primarily associated with their bulk properties and negligibly affected by surface phenomena.^{12,13} Moreover, the sub-wavelength dimensions of HNPs lift the spectral limitations imposed by phase-matching conditions in bulk nonlinear crystals, enabling wide tunability of excitation light and emission of multiple signals at once. Some research groups are also working on the efficiency enhancement of the optical properties by engineering hybrid systems based on a HNP-core and a plasmonic-shell tailored for specific spectral resonances.^{14,15}

Recently, we have demonstrated that the simultaneous emission of Second and Third Harmonic Generation (SHG, THG) by bare individual Bismuth Ferrite (BiFeO₃, BFO) HNPs can be easily acquired.¹⁶ We showed that the coincident acquisition of both harmonics can strongly benefit to imaging selectivity in optically congested environments¹¹ for applications like cell-tracking over long time in tissues.¹⁷ Besides harmonic generation, one can expect that high $\chi^{(n)}$ values by HNPs can be exploited for disposing of localized sources of long wavelength radiation by optical rectification¹⁸ or for generating nonclassical states of light.¹⁹⁻²¹ In this respect, the possibility of working efficiently at telecom wavelengths (1.5 μm) undeniably constitutes an asset for a future integration of HNPs as frequency conversion elements and all-optical logic operators²² in photonics cir-

cuits.

In this work, we demonstrate that second, third, and fourth harmonic (FHG) generated by an individual BFO HNP upon excitation at 1560 nm by an Erbium-doped fiber oscillator can be easily detected. Moreover, we show how the polarization control of excitation light allows tuning the relative intensities of the three harmonics leading to on demand modulation of the red, green, and blue (RGB) components of the emission. The simultaneous acquisition of three harmonics from the same nano-object is an *unicum* to date and, besides all the applications we mentioned, HNPs might assume the role of model system for the study of the interplay among multiple-harmonics and high harmonic generation in solids.²³⁻²⁶

I. MATERIALS AND METHODS

BFO nanoparticles synthesized by the company FEE GmbH (Idar-Oberstein, Germany) were obtained as a water stabilized colloidal suspension from the company TIBIO (Comano, Switzerland) under a research agreement. The average size is estimated to 100 nm by dynamic light scattering (DLS) and transmission electron microscopy (see Fig. S.I. 1). The extinction spectrum of particles dispersed in a polymer matrix is reported in Fig. S.I. 2. For imaging, a drop of BFO suspension is cast onto a microscope substrate and the solvent let evaporating.

As reported in Fig. 1, the light source of the set-up is a Telecom femtosecond fiber laser at 1560 nm with a repetition rate of 100 MHz and 100 mW average power (*T-Light FC*, Menlo Systems). Pulses are compressed down to 90 fs by an optical fiber connected at the laser output. At the fiber output, the beam is collimated in the free space and expanded to a diameter of 6 mm. For polarization resolved studies, the linear polarization of the laser is rotated by a $\lambda/2$ plate mounted on a motorized rotation stage. In the case of power dependence measurements, the laser energy is continuously modulated

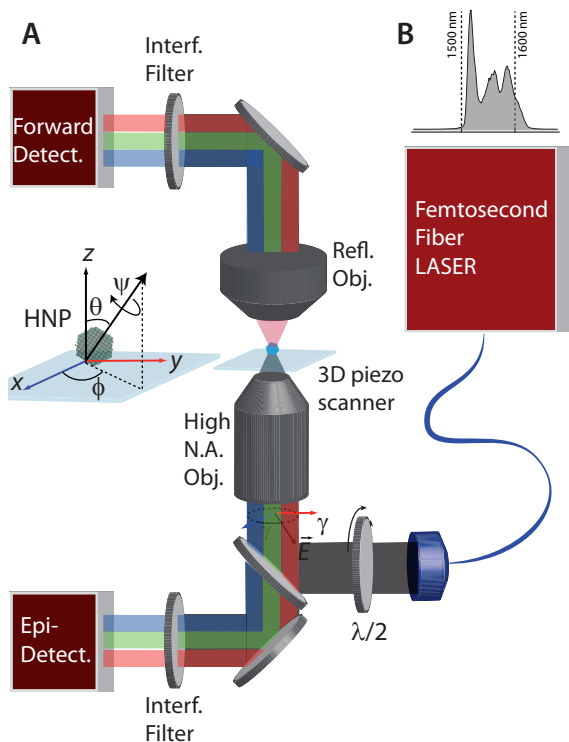


FIG. 1: **A.** Schematics of the experimental set-up. Not shown: a spectrometer can be inserted in the forward detection arm and interference filters removed for acquiring spectrally resolved traces. **B.** Measured laser emission spectrum.

through the succession of a $\lambda/2$ plate and a polarisation analyser. Afterwards, the beam is reflected by a 45 degrees short-pass filter (Chroma) and focused on a single isolated HNP by a $100 \times$ microscope oil immersion objective (NA 1.3). The signal generated by the particles is either epi- either forward-detected. In the latter case, the collection objective is a $40 \times$ N.A. 0.6 Schwarzschild aluminium coated reflective objective (Edmund optics). HNPs are selected by scanning a (x, y) planar ROI of approximately $20 \times 20 \mu\text{m}^2$ with a piezo-stage and carefully adjusting the z position by maximizing their non-linear signal. Both for epi- and forward-detection, narrow bandwidth interference filters are used to select the harmonic spectral region (Thorlabs *FBH780-10* for SHG, *FBH520-40* for THG, *FBH400-40* for FHG and Semrock *BrightLine Fluorescence Filter 387/11* for FHG). Additionally, a scanning spectrometer (*Acton SP2300*, Princeton Instruments, 300 g/mm) is placed in the forward detection arm to acquire spectrally resolved traces. The measurements are obtained using two different Hamamatsu detectors, selected according to their spectral response: *H7732-01* low noise side-on photomultiplier tube (185 nm to 680 nm), and *H7421-50* photon counting head with a GaAs photocatode (380 nm to 890 nm). Alternatively, we use a ultra-low-noise single photon counting module (*SPD-A-VISNIR*, Aurea Technology, Besançon,

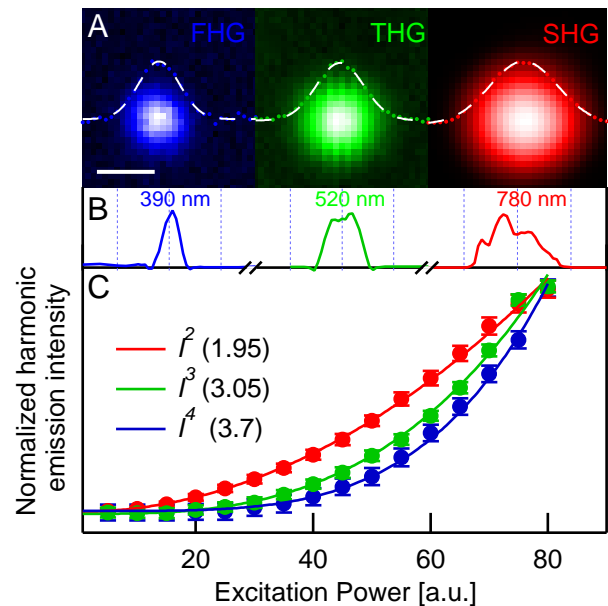


FIG. 2: **A.** Images taken at the different harmonics of a single isolated BFO HNP. The particle diameter is fitted by a Gaussian function (dashed lines). Scale bar 500 nm. Scale bar 1 μm . **B.** Harmonic spectra. The interval between two dashed vertical lines corresponds to 30 nm. **C.** Power dependence of the three harmonic normalized at the values obtained at the maximum excitation power. The continuous lines represent the I^n traces with $n = 2, 3, 4$. The optimal n values obtained by fitting the experimental traces are reported in parentheses.

France). For comparing relative intensities of the harmonics we took in full account the spectral sensitivity of the different detectors, and the spectral transmittance of all optical components measured using a spectrophotometer (*Lambda 20*, Perkin Elmer).

II. RESULTS AND DISCUSSION

The starting evidence motivating this work is the observation that a single BFO HNP deposited on a substrate in the focus of the laser emits simultaneously at the three harmonics as from the images in Fig. 2A. The heat-maps colors are chosen according to the actual emission, namely red for SHG (780 nm), green for THG (520 nm), and blue for FHG (390 nm). In the following, we first present a thorough assessment demonstrating by independent experimental observables (i) image spot size, ii) spectrum, and iii) excitation intensity dependence) that the three emission are genuinely associated with different nonlinear orders. Successively, we discuss the polarization-resolved emissions at the different orders which sheds light on the tensorial properties of the nonlinear susceptibilities and can be exploited for selective frequency up-conversion from short-wave infrared to the visible.

i) The Gaussian fits to the diameters of the particle images in Fig. 2A indicate that the FWHM decreases with increasing nonlinearity, as one expects for a diffraction limited object smaller than the point spread function (PSF) at the highest order. The widths of the PSF range from 673 nm for SHG to 486 nm for THG and 420 nm for FHG (see further details in S.I.). The average dimensions of the HNPs (≈ 100 nm) remain therefore out of reach at all orders. ii) In Fig. 2B, we provide the harmonic spectra detected in the forward direction. In the wavelength domain, one expects the width of the emission to scale as $\propto \frac{1}{n\sqrt{n}}$, with n being the nonlinear order.²⁷ This formula is derived for Gaussian pulses in the time domain. Therefore, to apply this estimation to our traces stemming from a structured spectral profile at the excitation wavelength (see Fig. 1B), we proceeded by fitting the broadest Gaussian curve supported by the excitation and by each harmonic spectrum. This way, we obtained widths for the different harmonics within 6% from the theoretical estimation. This result points to a rather complete upconversion of the frequencies in the fundamental spectrum and it is consistent with the fact that BFO HNPs are smaller than the coherence lengths for each nonlinear order, $l_c^{(n)}$. By using the optical con-

stants of BFO derived by Kumar *et al.*²⁸ and applying the full calculation including the effect of Gouy phase developed by Cheng and Xie²⁹ we obtain $l_c^{(n)}$ values in the forward direction spanning from 1 μm for $n = 2$ to 0.325 and 0.23 μm for $n = 3$ and 4, respectively and therefore larger than HNPs typical dimensions at all orders. This implies that no destructive interference takes place within the particle volume. iii) To complete this preliminary assessment of multiorder response, in Fig. 2C, we present the harmonic signal strength as a function of the laser intensity at the sample, I . The experimental datasets are normalized to their maximum value. The nominal curves (*i.e.*, I^n , $n = 2, 3, 4$) are plotted as continuous lines. One can appreciate their fairly good agreement with the experimental data. In the plot legend we also indicate the optimal values for the exponent n obtained letting this parameter free to vary in the fitting procedure. The retrieved values are all within 10% from the theoretical values. Altogether these results obtained by independent measurements (nonlinear PSF, harmonic spectra, intensity dependence) unambiguously support the association of the signals from single HNPs with three different harmonics: SHG, THG, and FHG.

Material	Intensity [GW/cm ²]	Exc. λ [nm]	SHG/THG [SHG/FHG]	Method	Ref.
KNbO ₃	11	1064	322	HRS	Schmidt <i>et al.</i> ¹⁶
BFO	650	1250	37	Microscopy	Rogov <i>et al.</i> ³⁰
BFO	11	1064	30	HRS	Schmidt <i>et al.</i> ¹⁶
ZnO	100	1350	4	NPs on substrate	Dai <i>et al.</i> ³¹
ZnO	400	1350	0.84	NPs on substrate	Dai <i>et al.</i> ³¹
BFO	370	1560	$(2 \pm 0.7) \times 10^{-3}$	Microscopy	this work
BFO	370	1560	[12 \pm 4]	Microscopy	this work

TABLE I: Experimental ratios between harmonic orders for different HNPs from literature and from this work.

A natural question arises concerning the relative intensities of the three emissions, as one would normally expect a major decrease in signal strength with increasing nonlinear rank, provided that the symmetry requirements (*i.e.*, noncentrosymmetry) are fulfilled for the generation of even orders (SHG, FHG,...). Clearly, one should also take into proper account the different intensity dependence exhibited by signals associated with each $\chi^{(n)}$. Higher excitation intensity is expected to favour higher orders as the ratio of two successive harmonics scales as $\propto \frac{1}{I}$. In table I we indicate the SHG/THG values reported in the literature for different nanomaterials along with the estimations we derived in this work for SHG/THG and SHG/FHG. We provide for each entry the excitation wavelength and intensity along with the experimental method used for the estimation. Note that, among all techniques, the values extracted by microscopy present a larger uncertainty because they imply averaging particles with different spatial orientations

modulating their harmonic ratios.¹⁶ Although the excitation settings and the ratio values reported in the table are quite sparse, one can definitively derive some trends. i) For the same material and same excitation wavelength, SHG/THG decreases with increasing intensity (ZnO). ii) Different materials present very different signal ratios under exactly the same excitation conditions (KNbO₃ and BFO). iii) Specific sample resonances seem to play an important role in determining the value of these ratios. For instance, for the BFO case, increasing the excitation wavelength favours the THG over the SHG emission. This observation most probably arises from the fact that the THG frequency lies very close to an absorption band in the material. The latter appears at around 445 nm according to the extinction spectrum in Fig. S.I. 2 and consistently with measurements on BFO 25 nm thin films.²⁸ Such a band in the visible region does not appear for ZnO and KNbO₃ HNPs, which start absorbing in the ultraviolet below 350 nm. This close-to-resonance condi-

tion can also help explaining the very high second order susceptibility reported for BFO HNPs excited at 1064 nm, which was estimated to 160 pm/V.^{16,32} Here, working at 1560 nm, we observe a very strong THG emission (visible by naked eye on micrometer aggregates!) and a comparatively weak SHG intensity (SHG/THG $\approx 10^{-3}$), likely because SHG is now spectrally far away from any resonance in the sample. The same way of reasoning supports the efficient production of FHG by 1560 nm excitation. The FHG intensity is in fact only one order of magnitude smaller than SHG in strength under our experimental conditions.

The high conversion efficiencies at the third and fourth order we observe for a noncentrosymmetric material displaying very high quadratic nonlinearity such as BFO, can be potentially ascribed to the presence of multi-step (cascading) processes involving a succession of purely $\chi^{(2)}$ phenomena: SHG and sum frequency mixing.²⁶ In this case, THG would *also* result from $\omega + \omega = 2\omega$ and $\omega + 2\omega = 3\omega$,³³ whereas FHG from $\omega + \omega = 2\omega$ and $2\omega + 2\omega = 4\omega$ or, alternatively, from $\omega + \omega = 2\omega$ followed by $2\omega + \omega = 3\omega$ and $3\omega + \omega = 4\omega$.³⁴ It is tempting to attribute the comparatively low emission at 2ω to a depletion of this frequency used as intermediate field for generating 3ω and 4ω , however discerning multi-step from direct higher order nonlinear processes is a complex task, in particular for nanoparticles as the absence of macroscopic propagation excludes discrimination methods based on phase-matching criteria.³³ The use of HNPs with controlled size and narrow size distribution or epitaxial thin films of variable thickness could help elucidating this aspect in a future series of experiments. These experiments should be performed using a tunable excitation to disentangle the effects of spectroscopic resonances from those associated with cascading.

In Fig. 3A, we introduce the results on polarization dependence for two sub-diffraction limited and isolated particles: HNP1 and HNP2. The shaded regions display the intensity of the harmonic emission detected as a function of the polarization angle of the excitation laser, γ . Note that differently from other works,^{16,35,36} in this case no polarization analyser was set in the detection arm. The differences between the response of the two HNPs are associated with the different spatial orientations of their crystal axis with respect to the laboratory frame (Euler angles ϕ, θ, ψ in Fig. 1). The simple inspection of the polarization resolved traces can provide interesting information. In general, the SHG traces possess a structure characterized by two dominant lobes in agreement with our previous observations.¹⁶ For THG and FHG the side lobes become more prominent. Interestingly, the orientation of the main lobes is maintained among the even orders (SHG, FHG) while for THG it seems that other tensor elements become predominant with major changes in orientation and symmetry. In our previous study, starting from a known $\chi^{(2)}$ tensor,²⁸ we fitted the orientation of several BFO particles and then used the retrieved Euler angles to determine the unknown

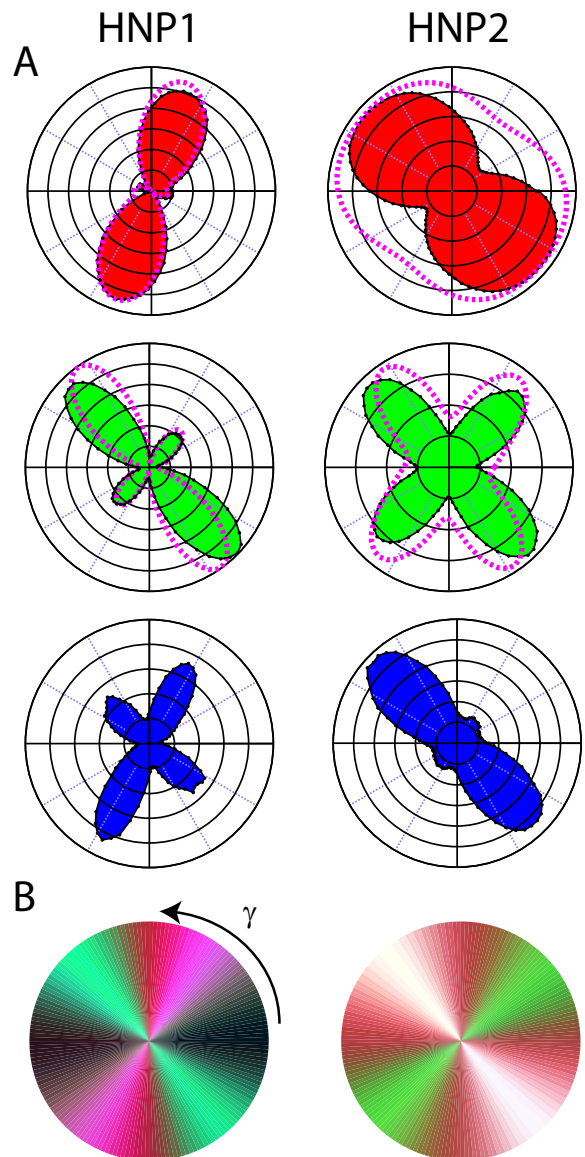


FIG. 3: **A.** The shaded regions represent the polarization resolved emission intensity at the different harmonic orders from two isolated BFO HNPs as a function of the polarization angle γ . The dashed purple lines are fits to the traces obtained using the $\chi^{(2)}$ and $\chi^{(3)}$ tensors reported in Schmidt *et al.*¹⁶ for 1064 nm excitation. The retrieved Euler angle (ϕ, θ, ψ) are ($78^\circ, 38^\circ, 314^\circ$) for HNP1 and ($68^\circ, 13^\circ, 77^\circ$) for HNP2. **B.** Alternative representation to highlight the selective frequency generation obtained by varying the polarization angle γ . The images are created by adding as RGB components the normalized SHG, THG, and FHG polarization-resolved traces in A.

$\chi^{(3)}$ tensor elements by simultaneously fitting the THG response of several HNPs.¹⁶ Here, we use these tensor values for $\chi^{(2)}$ and $\chi^{(3)}$ to fit the SHG and THG traces and obtain the Euler angles of each particle. The fits are reported as purple dashed lines on the data and the angle sets for HNP1 and HNP2 provided in the figure caption.

Although the fits correctly capture the main features of the polarization curves (main lobes angles, presence of orthogonal lobes), one should be aware that this procedure implies several approximations and the result should be considered qualitative in nature and primarily intended to support the fact that the BFO point group ($3m$) is compatible with the observed traces. In particular, the tensors we apply are derived at 1064 nm and not at 1560 nm. Note also that we could not readily extend this approach to $\chi^{(4)}$ because the number of independent elements of this tensor prevents the retrieval of a reliable outcome. As a last *caveat*, we highlight that the possible presence of competing multi-step $\chi^{(2)}$ processes would undermine the general validity of this description, which would remain however an effective tool for predicting the polarization dependent response of BFO HNPs even in presence of concurrent direct and cascaded generation.

Interestingly, the response of the two randomly oriented HNPs suggests that the choice of the excitation polarization, even in absence of any detection analyser, can be used to modulate the relative intensities of the three emissions for a given laser polarization angle γ . In Fig. 3B, we graphically emphasize this procedure showing the emission color obtained by adding the normalized polarization dependent RGB components displayed by HNP1 and HNP2. This representation shows how, for a given HNP orientation, specific values of γ are associated with strong simultaneous SH, TH, FH emission (white regions), with individual harmonics (red, green, blue) and combination thereof (purple, pink...) or low emission (dark regions). We speculate that this approach could be adapted to precisely oriented BFO HNPs and thin films with thickness smaller than the shortest coherence length to provide polarization-controlled frequency converters from the telecom region over the visible spectrum. Engineered hybrid structures composed by HNPs with a plasmonic shell of tailored thickness could be a way to mitigate the conversion efficiency differences at the three harmonic orders for defined applications.^{14,15} Alternatively, the nonlinear sensitivity of the response of the HNPs to critical pulse parameters (intensity, duration, polarization) can be exploited in fiber sensors.³⁷

III. CONCLUSIONS

In conclusion, we have reported what to our best knowledge is the first demonstration of simultaneous ac-

quisition of three harmonic frequencies generated by a single nanoobject with a size of the order of 100 nm. Notably, our experiment is performed using a fiber laser at telecom wavelength, which holds great promise for implementing this frequency conversion approach in optoelectronic circuitry. Considered the novelty of our observation, we first thoroughly assessed the spectral and imaging properties and the intensity dependence of the emissions to ensure that they are genuinely associated with frequency conversion by $\chi^{(n)}$, $n = 2, 3, 4$ or cascaded $\chi^{(2)}$ processes and that no spurious signals are present in the emission. The relative intensities of the three harmonics have been estimated for BFO under these excitation conditions indicating extremely high efficiency, in particular for THG. Finally, we have discussed the excitation-polarization dependence of the particle emission, demonstrating that this approach opens the way to directly investigating the interplay among nonlinear susceptibility tensors elements at different orders and modulating the relative strengths of RGB components for photonics applications.

IV. ACKNOWLEDGEMENTS

We acknowledge the financial support by Swiss SEFRI (project C15.0041, Multi Harmonic Nanoparticles), and the French-Switzerland Interreg programme (project NANOFIMT). This study was performed in the context of the European COST Action MP1302 Nanospectroscopy. We are grateful to Dr. Davide Staedler at TIBIO SA (Comano, Switzerland) and Dr. Daniel Rytz at FEE GmbH (Idar-Oberstein, Germany) for synthesizing and providing us colloiddally stable BFO HNPs, to Dr. Johann Cussey from Aurea Technology (Besançon, France) for providing us the the single photon counting module and technological support, and Mathias Urbain (SYMME, Annecy) and Virginie Monnier (Institut des Nanotechnologies, Lyon) for the TEM images of BFO HNPs.

¹ Kauranen, M.; Zayats, A. V. *Nature Photonics* **2012**, *6*, 737–748.

² Dadap, J. I.; Shan, J.; Eisenthal, K. B.; Heinz, T. F. *Physical Review Letters* **1999**, *83*, 4045.

³ Butet, J.; Duboisset, J.; Bachelier, G.; Russier-Antoine, I.; Benichou, E.; Jonin, C.; Brevet, P.-F. *Nano letters* **2010**, *10*, 1717–1721.

⁴ Lippitz, M.; van Dijk, M. A.; Orrit, M. *Nano letters* **2005**, *5*, 799–802.

⁵ Danckwerts, M.; Novotny, L. *Physical Review Letters* **2007**, *98*, 026104.

⁶ Jacobsohn, M.; Banin, U. *The Journal of Physical Chemistry B* **2000**, *104*, 1–5.

⁷ Bar-Elli, O.; Grinvald, E.; Meir, N.; Neeman, L.; Oron, D.

- ACS nano* **2015**, *9*, 8064–8069.
- ⁸ Dean, J. J.; van Driel, H. M. *Applied Physics Letters* **2009**, *95*, 261910.
 - ⁹ Hong, S.-Y.; Dadap, J. I.; Petrone, N.; Yeh, P.-C.; Hone, J.; Osgood Jr, R. M. *Physical Review X* **2013**, *3*, 021014.
 - ¹⁰ Kumar, N.; Najmaei, S.; Cui, Q.; Ceballos, F.; Ajayan, P. M.; Lou, J.; Zhao, H. *Physical Review B* **2013**, *87*, 161403.
 - ¹¹ Rogov, A.; Irondelle, M.; Ramos Gomes, F.; Bode, J.; Staedler, D.; Passemard, S.; Courvoisier, S.; Yamamoto, Y.; Waharte, F.; Ciepielewski, D. *ACS Photonics* **2015**, *2*, 1416–1422.
 - ¹² Staedler, D. et al. *Acs Nano* **2012**, *6*, 2542–2549.
 - ¹³ Kim, E.; Steinbrück, A.; Buscaglia, M. T.; Buscaglia, V.; Pertsch, T.; Grange, R. *ACS nano* **2013**, *7*, 5343–5349.
 - ¹⁴ Pu, Y.; Grange, R.; Hsieh, C. L.; Psaltis, D. *Physical Review Letters* **2010**, *104*.
 - ¹⁵ Richter, J.; Steinbrück, A.; Zilk, M.; Sergeev, A.; Pertsch, T.; Tnnermann, A.; Grange, R. *Nanoscale* **2014**, *6*, 5200–5207.
 - ¹⁶ Schmidt, C.; Riporto, J.; Uldry, A.; Rogov, A.; Mugnier, Y.; Le Dantec, R.; Wolf, J.-P.; Bonacina, L. *Scientific reports* **2016**, *6*.
 - ¹⁷ Dubreil, L.; Leroux, I.; Ledevin, M.; Schleder, C.; Lagalice, L.; Lovo, C.; Fleurisson, R.; Passemard, S.; Kilin, V.; Gerber-Lemaire, S. *ACS nano* **2017**, *11*, 6672–6681.
 - ¹⁸ Polyushkin, D.; Hendry, E.; Stone, E.; Barnes, W. *Nano letters* **2011**, *11*, 4718–4724.
 - ¹⁹ Grice, W. P.; Walmsley, I. A. *Physical Review A* **1997**, *56*, 1627.
 - ²⁰ Dot, A.; Borne, A.; Boulanger, B.; Bencheikh, K.; Levenson, J. *Physical Review A* **2012**, *85*, 023809.
 - ²¹ Wu, L.-A.; Kimble, H.; Hall, J.; Wu, H. *Physical review letters* **1986**, *57*, 2520.
 - ²² Puddu, E.; Allevi, A.; Andreoni, A.; Bondani, M. *JOSA B* **2004**, *21*, 1839–1847.
 - ²³ Ghimire, S.; DiChiara, A. D.; Sistrunk, E.; Agostini, P.; DiMauro, L. F.; Reis, D. A. *Nature physics* **2011**, *7*, 138–141.
 - ²⁴ Vampa, G.; Hammond, T.; Thiré, N.; Schmidt, B.; Légaré, F.; McDonald, C.; Brabec, T.; Corkum, P. *Nature* **2015**, *522*, 462–464.
 - ²⁵ Luu, T. T.; Wörner, H. J. *Physical Review B* **2016**, *94*, 115164.
 - ²⁶ Saltiel, S. M.; Sukhorukov, A. A.; Kivshar, Y. S. *arXiv preprint nlin/0311013* **2003**,
 - ²⁷ Ehmke, T.; Knebl, A.; Reiss, S.; Fischinger, I. R.; Seiler, T. G.; Stachs, O.; Heisterkamp, A. *AIP advances* **2015**, *5*, 084903.
 - ²⁸ Kumar, A.; Rai, R. C.; Podraza, N. J.; Denev, S.; Ramirez, M.; Chu, Y.-H.; Martin, L. W.; Ihlefeld, J.; Heeg, T.; Schubert, J. *Applied Physics Letters* **2008**, *92*, 121915.
 - ²⁹ Cheng, J.-X.; Xie, X. S. *JOSA B* **2002**, *19*, 1604–1610.
 - ³⁰ Rogov, A. et al. *ACS Photonics* **2015**, *2*, 1416–1422.
 - ³¹ Dai, J.; Yuan, M.-H.; Zeng, J.-H.; Dai, Q.-F.; Lan, S.; Xiao, C.; Tie, S.-L. *Applied optics* **2014**, *53*, 189–194.
 - ³² Schwung, S.; Rogov, A.; Clarke, G.; Joulaud, C.; Magouroux, T.; Staedler, D.; Passemard, S.; Justel, T.; Badie, L.; Galez, C. *Journal of Applied Physics* **2014**, *116*, 114306.
 - ³³ Bosshard, C.; Gubler, U.; Kaatz, P.; Mazerant, W.; Meier, U. *Physical Review B* **2000**, *61*, 10688–10701.
 - ³⁴ Ivanov, R.; Saltiel, S. *JOSA B* **2005**, *22*, 1691–1698.
 - ³⁵ Brasselet, S.; Le Floc’h, V.; Treussart, F.; Roch, J. F.; Zyss, J.; Botzung-Appert, E.; Ibanez, A. *Physical Review Letters* **2004**, *92*.
 - ³⁶ Bonacina, L.; Mugnier, Y.; Courvoisier, F.; Le Dantec, R.; Extermann, J.; Lambert, Y.; Boutou, V.; Galez, C.; Wolf, J. P. *Applied Physics B-Lasers and Optics* **2007**, *87*, 399–403.
 - ³⁷ López-Higuera, J. M.; Cobo, L. R.; Incera, A. Q.; Cobo, A. *Journal of lightwave technology* **2011**, *29*, 587–608.

Supplementary information

A. Transmission Electron Microscopy images of BFO HNPs

In Fig. S.I.1 we provide a transmission electron microscopy image of the BFO HNPs used in this work.

B. Extinction spectrum

The spectrum in Fig. S.I.2 was acquired on BFO HNPs dispersed in Poly(methyl methacrylate) at 0.5 mg/ml concentration. The resonance peak discussed in the main text is indicated by the arrow.

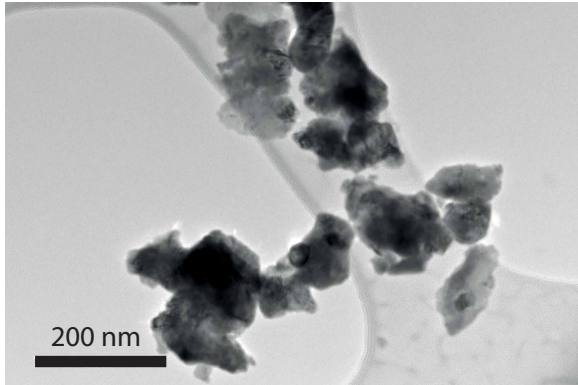


FIG. 1: TEM image of BFO HNPs.

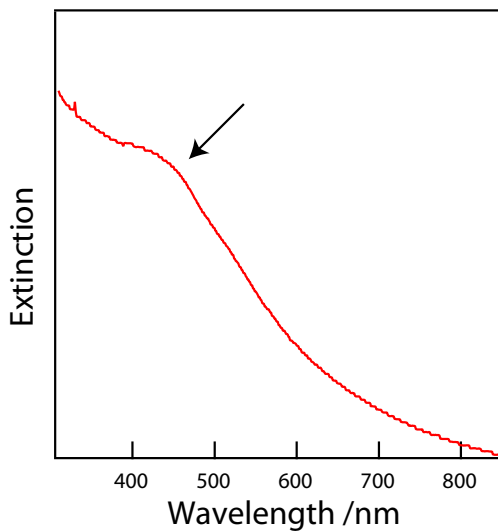


FIG. 2: Extinction spectrum of BFO HNPs.

C. Fit of the Point Spread Function (PSF) at the different harmonic orders

Taking into account excitation wavelength and objective numerical aperture, the nominal resolution of the imaging system under linear excitation should be 600 nm. However, the resolution is expected to be severely reduced by the fact that we are using an high NA oil immersion objective conceived for the visible region, therefore all aberration corrections and optical elements (comprising the matching medium) are far from optimal. Indeed, we observe an energy reduction of 75% upon laser transmission through this objective, indicating a poor compatibility at this wavelength. By considering that the resolution should be proportional to $1/\sqrt{n}$ where n is the nonlinear order, we can readily compute an actual value of 842 nm for the width of the linear PSF, by multiplying the FHG FWHM by $\sqrt{4}$ and the THG one by $\sqrt{3}$. The same approach applied to the SHG FWHM provides a result 12% higher. This discrepancy comes from the deviation from linear response of the detector used for SHG in this series of measurements.